11th International Symposium on Magnetic Bearings
August 26-29, Nara, Japan

BEARINGLESS SEGMENT MOTOR WITH BURIED MAGNETS

Wolfgang Gruber
Institute of Electrical Drives and Power Electronics, Johannes Kepler University, Linz, Austria
wolfgang.gruber@jku.at

Wolfgang Amrhein
Institute of Electrical Drives and Power Electronics, Johannes Kepler University, Linz, Austria
Austrian Center of Competence in Mechatronics (ACCM)
wolfgang.amrhein@jku.at

Thomas Stallinger
Institute of Electrical Drives and Power Electronics, Johannes Kepler University, Linz, Austria
thomas.stallinger@students.jku.at

ABSTRACT
Bearingless motors combine contactless levitation and rotation in a preferably compact system design, because the bearing as well as motor windings are located on the same lamination stack. By the use of a proper control scheme and the superposition of different current components, bearing forces and motor torque can be generated simultaneously by applying concentrated windings. This leads to a further simplification of the mechanical configuration. The bearingless segment motor features such concentrated coils on separated stator elements, which reduce the stator iron and therefore weight and cost, especially for constructions with large diameters.

However, most of the bearingless motors are designed with surface mounted permanent magnets on the rotor, neglecting the advantages of buried permanent magnets. In this paper a bearingless segment motor with buried permanent magnets is investigated. The mathematical model is presented, a proper control scheme is introduced and the optimization of the prototype motor is outlined. Some motor specific considerations concerning the angular sensors and the rotordynamic are also given. Finally, the performance of the bearingless segment motor with buried permanent magnets is shown by the comparison of simulation results with measurement data of the manufactured prototype.

INTRODUCTION
The advantages of bearingless drives are evident. Contactless levitation leads to wearless and lubrication free operation. Furthermore the rotating part and the stator can be separated completely by the use of a rotor can. This leads to hermetically sealed systems which can satisfy high demands on cleanliness, chemical resistance and tightness. Therefore such motors are often employed in the pharmaceutical, biomedical, chemical, semiconductor or aerospace industry.

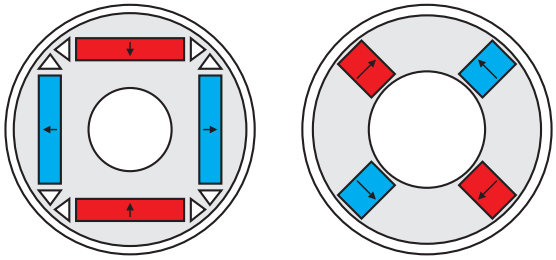

FIGURE 1: Classical rotor designs featuring buried magnets

Bearingless systems have to stabilize all six degrees of freedom by magnetic forces. In general these systems show a quite complex build-up. The bearingless slice motor [1] reduces the system complexity because three degrees of freedom (tilting and axial direction) are passively stabilized by means of reluctance forces. This becomes possible due the permanent magnet excited disc shaped rotor. In the recent past the bearingless segment motor was introduced [2] as a subtype of the bearingless slice motor.

However, a lot of these bearingless motors [3], [4] feature just one magnetic pole pair in the rotor. So a surface mounted permanent magnet ring with a diametric magnetization is utilized. This approach is no longer possible for a higher number of pole pairs. In these cases surface mounted magnet segments are often used [6], [7]. These arrangements request a kind of bandage to fasten the magnets to the rotor surface at high circumferential velocity. In contrast buried magnets are fixed by the rotor iron itself [5]. Figure 1 shows the two most familiar rotor types with buried magnets. One features a tangential, the other a radial

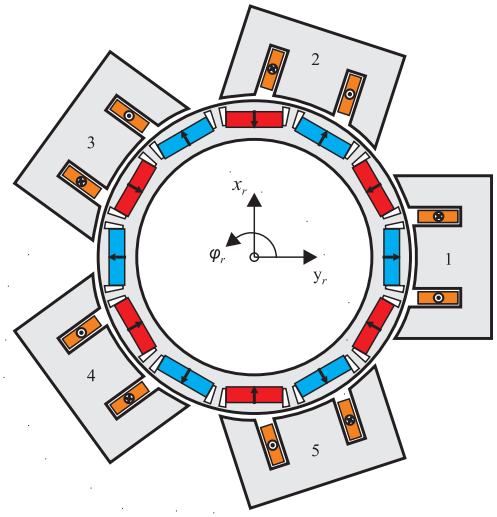

FIGURE 2 Drawing of the bearingless segment motor with buried magnets

magnetization. The small bars bypass the magnetic flux and are assumed to be in saturation. Though these bars reduce the magnetic main flux over the air gap, they are needed to increase the mechanical coherence of the rotor. Inexpensive rectangular magnet segments can be used, which are easily assembled to the rotor in addition. The armature reaction increases when buried magnets are used due to the smaller effective magnetic air gap. This fact also leads to a good capability for field weakening, resulting in a higher idle speed of the buried magnet motor. It is also obvious from Figure 1 that the inductance of the stator coils will generally depend from the rotor angle.

In this paper a bearingless segment motor with five stator elements and a rotor holding buried magnets with radial magnetization is discussed. The chosen number of pole pairs in the rotor is six. It is feasible to implement a bearingless motor with just three stator segments, but this demands for a power electronic with three full bridges (12 transistors). Segment motors with four stator elements can work with eight transistors, but show some disadvantages in the operating behaviour. Therefore it was decided to implement a motor with five stator segments and a power electronic using ten switching elements. Stator elements featuring three pole shoes with concentrated windings simultaneously create bearing forces and motor torque. Figure 2 shows a schematic drawing of the assembly.

CONTROL SCHEME

In this chapter the mathematical model and a proper control scheme is presented in brief. To simplify matters only the model for current injection is given here. In addition, eddy current, saturation and hysteresis effects are not considered. The detailed deduction and the more complex model for voltage injection can be found in [9].

Force and Torque

A description of the bearing forces (F_x, F_y) and the motor torque (M_z) of the system is given in [10] by

$$\begin{pmatrix} F_x(\mathbf{x_r}) \\ F_y(\mathbf{x_r}) \\ M_z(\mathbf{x_r}) \end{pmatrix} = \begin{pmatrix} \mathbf{i_s}^T & 0 & 0 \\ 0 & \mathbf{i_s}^T & 0 \\ 0 & 0 & \mathbf{i_s}^T \end{pmatrix} \mathbf{M_Q}(\mathbf{x_r})\mathbf{i_s} + \mathbf{M_L}(\mathbf{x_r})\mathbf{i_s} + \mathbf{M_N}(\mathbf{x_r}). \quad (1)$$

Here $\mathbf{x_r}=(x_r, y_r, \varphi_r)^T$ represents the rotor position by the axial deflections and rotor angle. The vector of the stator currents $\mathbf{i_s}=(i_{s1}, i_{s2}, i_{s3}, \ldots, i_{sn})^T$ is composed of the m phase currents. There is a quadratic ($\mathbf{M_Q}$), a linear ($\mathbf{M_L}$) and a term of no dependency ($\mathbf{M_N}$) concerning the stator currents. Considering rotors with surface mounted magnets the quadratic part is usually very small. By contrast this term can become considerable when buried magnets are used in the rotor, but only in case of high stator currents. Therefore this equation can be linearized via Taylor series approximation and yields to

$$\begin{pmatrix} F_x(\varphi_r) \\ F_y(\varphi_r) \\ M_z(\varphi_r) \end{pmatrix} = \mathbf{T_m}(\varphi_r)\mathbf{i_s} + \mathbf{T_c}(\varphi_r, \mathbf{i_s}) + \mathbf{K_x}(\varphi_r, \mathbf{i_S})\mathbf{x_r}. \quad (2)$$

Overall Model

Adding the mechanical equations of motion the overall model of the system with current injection is given by[1]

$$\dot{\mathbf{x}} = \begin{pmatrix} \mathbf{O_{3\times3}} & \mathbf{E_3} \\ \mathbf{M^{-1}}\,\mathbf{K_x}(\varphi_r, \mathbf{i_S}) & \mathbf{O_{3\times3}} \end{pmatrix} \mathbf{x} + \begin{pmatrix} \mathbf{O_{3\times m}} \\ \mathbf{M^{-1}}\,\mathbf{T_m}(\varphi_r) \end{pmatrix} \mathbf{i_S} + \begin{pmatrix} \mathbf{O_{3\times1}} \\ \mathbf{M^{-1}}\,\mathbf{T_c}(\varphi_r, \mathbf{i_S}) \end{pmatrix}, \quad (3)$$

with $\mathbf{i_s}$ as the actuating variable. The state vector $\mathbf{x}$ is defined as

$$\mathbf{x} = \begin{pmatrix} x_r & y_r & \varphi_r & \dot{x}_r & \dot{y}_r & \omega_r \end{pmatrix}^T. \quad (4)$$

In this equation of motion $\mathbf{M}$ represents the diagonal mass matrix and $\mathbf{K_x}(\varphi_r)$ the stiffness matrix, $\mathbf{T_m}(\varphi_r)$ is called current-force matrix and $\mathbf{T_c}(\varphi_r, \mathbf{i_S})$ is the reluctance matrix.

[1] $\mathbf{O}_{n\times m}$ represents a zero matrix of the dimension $n \times m$ and $\mathbf{E}_n$ stands for an identity matrix of the dimension n.

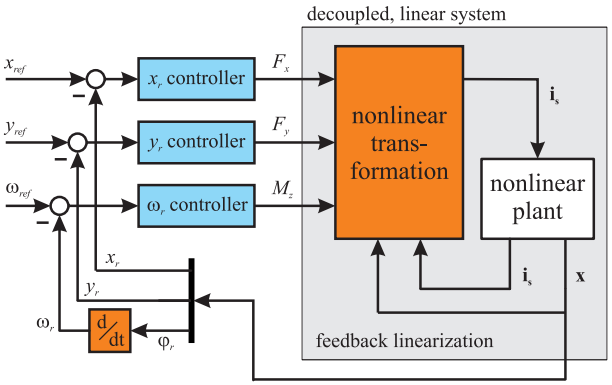

FIGURE 3 Overall control scheme

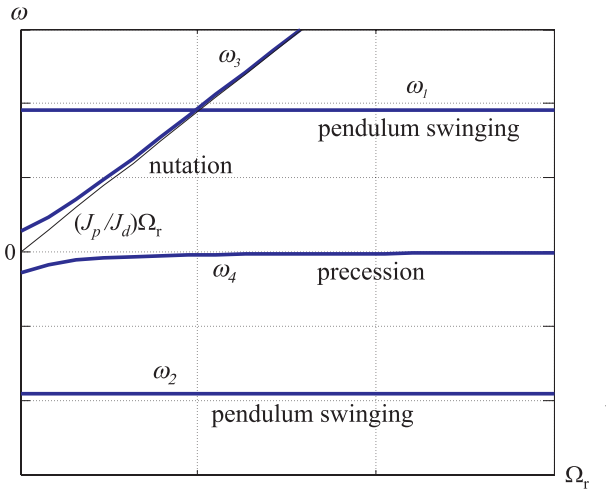

FIGURE 4 Map showing the critical speed

Control Scheme

For the deduced nonlinear model (3) a proper control scheme has to be found. A possible choice is to use nonlinear feedback techniques [9]. Utilizing the pseudo inverse matrix of $\mathbf{T_m}(\varphi_r)$, which is also called force-current matrix $\mathbf{K_m}(\varphi_r)$, it is possible to compensate all nonlinearities with an bias current vector, depending from the rotor angle and the current vector itself, leading to an overall linear and decoupled model

$$\dot{\mathbf{x}} = \begin{pmatrix} \mathbf{O}_{3\times3} & \mathbf{E}_3 \\ \mathbf{M}^{-1}\bar{\mathbf{K}}_x & \mathbf{O}_{3\times3} \end{pmatrix}\mathbf{x} + \begin{pmatrix} \mathbf{O}_{3\times m} \\ \mathbf{M}^{-1}\mathbf{T}_m(\varphi_r) \end{pmatrix}\mathbf{i}_S \,. \tag{5}$$

Details about the proposed approach can be found in [9]. The outer controllers for this model can be formulated using known design methods for linear time invariant systems. Often the use of simple PID or PD controllers is adequate enough to stabilize the radial position and to control the rotor speed. Figure 3 illustrates the general control scheme.

ROTOR DYNAMICS

A lot of bearingless systems feature low damping. On the one hand this is an advantage, because it means low system losses, but on the other hand it also implies certain sensitivity to resonance effects. Hence it is important to identify the critical speeds. If they are known, it is theoretically possible to detune the resonances by changing the stiffness due to the active control.

In this section the closed loop rotordynamic model for the bearingless slice motors is analyzed to compute the critical speeds. Using complex coordinates [11] for the rotor deflection

$$\underline{r} = x_r + j\,y_r \tag{6}$$

and the tilting

$$\underline{\varphi} = \beta_r - j\,\alpha_r \tag{7}$$

the rotordynamic model [12] is given by

$$\begin{pmatrix} m_r & 0 \\ 0 & J_d \end{pmatrix}\begin{pmatrix} \ddot{\underline{r}} \\ \ddot{\underline{\varphi}} \end{pmatrix} = \begin{pmatrix} 0 & 0 \\ 0 & j\,J_p\Omega_r \end{pmatrix}\begin{pmatrix} \dot{\underline{r}} \\ \dot{\underline{\varphi}} \end{pmatrix} - \begin{pmatrix} k_r & 0 \\ 0 & k_\varphi \end{pmatrix}\begin{pmatrix} \underline{r} \\ \underline{\varphi} \end{pmatrix}, \tag{8}$$

where m_r represents the rotor mass, J_d the diametral moment of inertia (in tilting direction), J_p the polar moment of inertia, k_r the radial stiffness and k_φ the tilting stiffness.

This model incorporates the closed loop equation of the radial rotor components from (5) with a proper PD controller and the appropriate equations in passively stabilized tilting directions. The mass is assumed to be a rigid body and damping is neglected. This leads to a model of an undamped, symmetrically and elastically supported Jeffcott or Laval rotor. Thus it is visible from the structure of the equation of motion (8) that the complex coordinates $\underline{r}$ an $\underline{\varphi}$ are decoupled.

Eigenvalues

The characteristic polynomial of (8) can be evaluated to

$$\begin{aligned} m_r J_d \lambda^4 - m_r J_p \Omega_r \lambda^3 - \left(m_r k_\varphi + J_d k_r\right)\lambda^2 \\ + J_p \Omega_r k_r \lambda + k_r k_\varphi = 0. \end{aligned} \tag{9}$$

The solution of this equation leads to four complex solutions and substituting λ=jω to the critical frequencies

$$\omega_{1,2} = \pm\sqrt{\frac{k_r}{m_r}} \tag{10}$$

and

$$\omega_{3,4} = \frac{J_p \Omega_r}{2J_d} \pm \sqrt{\left(\frac{J_p \Omega_r}{2J_d}\right)^2 + \frac{k_\varphi}{J_d}}\,. \tag{11}$$

Figure 4 shows the dependency of these values from the mechanical rotor angular velocity Ω_r. This chart is known as Campbell diagram.

There are two pendulum swingings, the nutation and the precession visible in that chart. For a real resonance, these modes have to be excited. A static unbalance in the rotor for example just excites ω_1, but not ω_2. For bearingless slice motors $J_p > J_d$ holds true in general, so dynamic unbalance will never excite ω_3 and ω_4. Thus, starting up an unbalanced bearingless slice motor there is only one critical speed to expect. In contrast higher harmonic excitations can lead to multiple critical speeds.

HALL-SENSOR SIGNALS

Hall sensors detect the magnetic field of the permanent magnets in the air gap to determine the electrical rotor angle. To get signals analog to common sin/cos encoders at least two sensors are needed. These couple of sensors have to be displaced by a mechanical angle of 90° divided by the number of pole pairs p_z. Hence the rotor angle is calculated by the arc tangent function. As a matter of fact the measured magnetic field of the Hall sensors have to be both sinusoidal.

However, using the buried magnet rotor geometry the measured magnetic flux is not absolute sinusoidal but contains higher harmonics. Furthermore it can be difficult to displace the sensors exactly 90° electrical with respect to the mechanical construction. The following analysis will give instructions where to place the sensor and how to transform the signals in order to suppress certain harmonics.

Sensor Signals

A non sinusoidal but periodic Hall sensor signal $B(\varphi_r)$ can be described by its harmonics in the form

$$B(\varphi_r) = \underline{\mathbf{\Omega}}(\varphi_r)^T \, \underline{\mathbf{b}} \tag{12}$$

with

$$\underline{\mathbf{\Omega}}(\varphi_r) = \begin{pmatrix} \cdots & e^{-j2\varphi_r} & e^{-j\varphi_r} & 1 & e^{j\varphi_r} & e^{j2\varphi_r} & \cdots \end{pmatrix}^T \tag{13}$$

and the infinite vector of complex Fourier coefficients

$$\underline{\mathbf{b}} = \begin{pmatrix} \cdots & \underline{b}_{-2} & \underline{b}_{-1} & \underline{b}_0 & \underline{b}_1 & \underline{b}_2 & \cdots \end{pmatrix}^T. \tag{14}$$

Due to the fact that the signal is unbiased, $\underline{b}_0$ is zero. Furthermore the coefficients $\underline{b}_{-i}$ and $\underline{b}_i$ are conjugate complex numbers.

Anyway, assuming a symmetrical placement of the m Hall sensors around the circumference of the air gap the measured signals can be described as

$$B_i(\varphi_r) = B\left(\varphi_r + \frac{2\pi p_z}{m} i\right) \quad i \in \mathbb{N} \,|\, 0 \le i \le m-1\,. \tag{15}$$

The announced symmetrical arrangement of the sensors is typical for the bearingless segment motor. Here m is equal to the number of phases of the motor, because it is advantageous to place the sensors in-between the stator segments to have a minimum disturbance due to the magnetic flux of the stator windings.

Transformation

The measured Hall sensor signals $B_i(\varphi_r)$ are now transformed into two components by

$$\begin{pmatrix} B_{0°}(\varphi_r) \\ B_{90°}(\varphi_r) \end{pmatrix} = V \begin{pmatrix} B_1(\varphi_r) & \cdots & B_{m-1}(\varphi_r) \end{pmatrix}^T \tag{16}$$

utilizing the constant transformation matrix

$$V = \begin{pmatrix} 0 & \cos\left(\frac{2\pi k}{m}\right) & \cdots & \cos\left(\frac{2\pi k(m-1)}{m}\right) \\ 1 & \sin\left(\frac{2\pi k}{m}\right) & \cdots & \sin\left(\frac{2\pi k(m-1)}{m}\right) \end{pmatrix} \tag{17}$$

where k is an optional integer. This mapping is known as generalized Clark transformation [8] and is used to mathematically reduce the phases in electrical rotating field machines (in that case k often equals 1).

Suppression of Harmonics

The analysis of equation (16) together with (12) leads to the following results for the first component

$$B_{0°}(\varphi_r) = \sum_{i=-\infty}^{\infty} \left[\underline{b}_i \cdot \sum_{z=0}^{m-1} \left(\cos\left(\frac{2\pi k z}{m}\right) e^{ji\left(\varphi_r + \frac{2\pi p_z z}{m}\right)} \right) \right]. \tag{18}$$

For the correctness of this equation the precondition of unbiased sensor signals must be met. Hence, it is obvious, that $B_{0°}(\varphi_r)$ and $B_{90°}(\varphi_r)$ possess the same harmonics, they just feature different phase shifts. This is explainable from the special composition of V. The coefficients of the first and second line each show a phase shift of 90°.

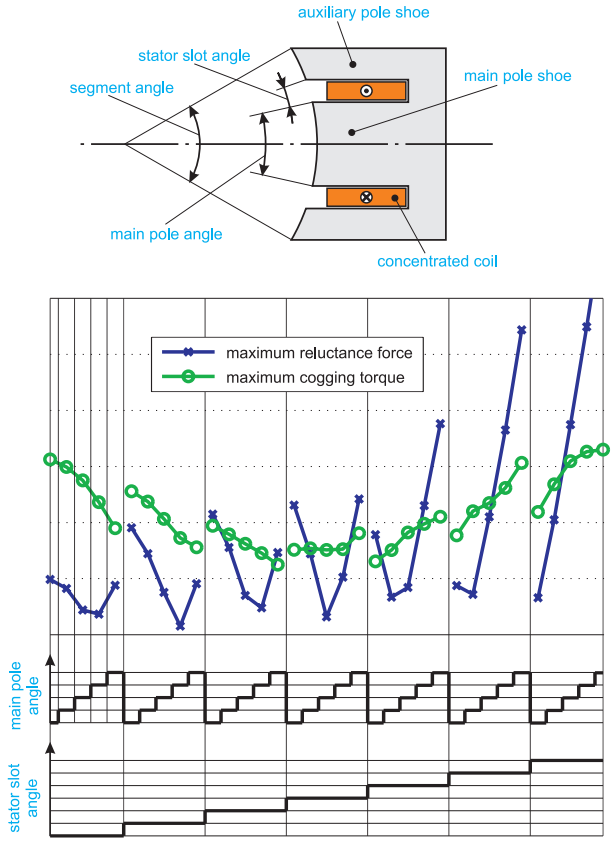

FIGURE 5 Stator element and finite element optimization

Taking a closer examination of (18) it turns out that a harmonic of the order i disappears, when the following relation

$$p_z\, i = n\, m \pm k \tag{19}$$

cannot be satisfied for any integer n. This fact allows a selective suppression of harmonics in the transformed coordinates. So with the appointed transformation the same sin/cos data interpretation can be done in the microprocessor for sensor signals with higher harmonics.

OPTIMIZATION

2D and 3D finite element simulations were carried out to optimize bearing forces and motor torque and to minimize the reluctance forces and the cogging torque. Both the rotor and the stator geometry were optimized. Due to a minimum required space for the sensors the stator segment angle is limited by 60°. For that range this segment angle features maximum bearing forces

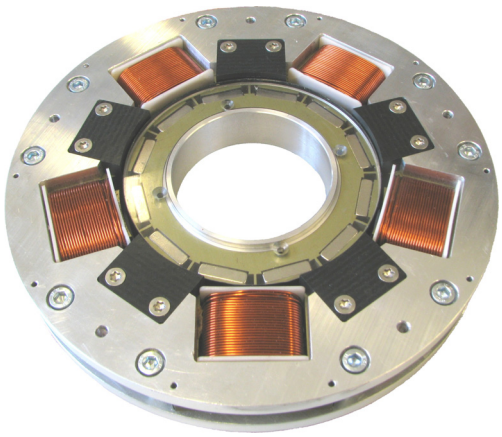

FIGURE 6 Bearingless segment motor prototype

and good motor torque. Furthermore, it also provides the best axial and tilting stiffness.

Figure 5 shows the analysis of a finite element simulation, where two parameters (main pole angle and stator slot angle) were varied to reduce the reluctance forces and the cogging torque. A main pole angle of 25° and a stator slot of 7mm were determinated. Because of calculating capacity and time economy these optimizations were done in 2D by Femag® and then exemplarily verified by Maxwell 3D®. Table 1 shows the characteristic data of the optimized motor.

MANUFACTURED MOTOR

To evaluate the functionality of the motor and the quality of the optimization a prototype was built, visible in Figure 6. The five stator elements (each holding a concentrated winding coil) are held among an aluminium framework. Inside the rotor the buried permanent magnets are cognizable, forming six magnetic pole pairs. The used Ni-coated NdFeB magnets feature a remanence field density B_r of 1.2T. The stator and rotor iron consist of laminated V270-35A steel plates.

TABLE 1 Characteristic data of the prototype motor

Rotor diameter	d_r	*99 mm*
Magnetic airgap	l_δ	*2.5 mm*
Max. magnetomotive force	d_r	*1200 AWdg.*
Axial stiffness	k_z	*7 N/mm*
Tilting stiffness	k_φ	*0.15 Nm/°*
Force capacity	F_r	*50 N*
Torque capacity	T_m	*2 Nm*

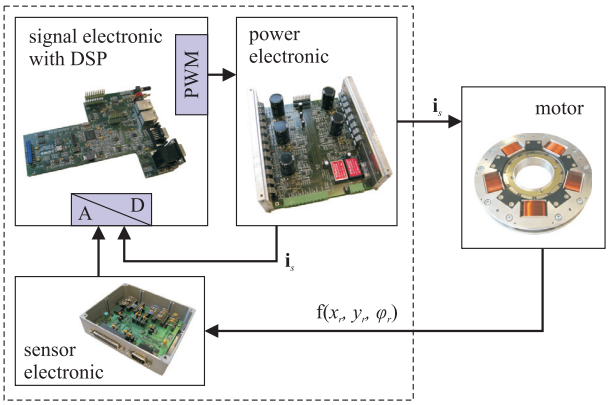

FIGURE 7 Components of the bearingless motor system

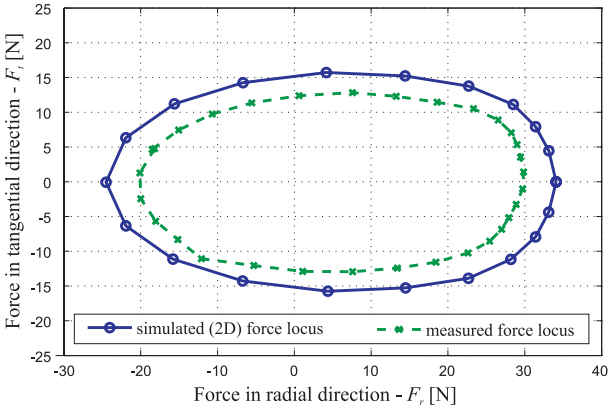

FIGURE 8 Force locus of one coil at constant rated current – simulated and measured

The control scheme was implemented on the inexpensive 16 bit fixed point digital signal processor family TMS320 by Texas Instruments. The processor is well integrated in the power electronics, featuring a maximum performance of 10A per phase at an intermediate direct current link of 70V. The software is written in ANSI C-code to alleviate modifications or extensions. The components of the whole system are visible in Figure 7. A sensor electronic was designed to evaluate the position sensors and to perform the transformation (16) of the Hall sensors.

MEASUREMENTS

To compare the characteristics of the built motor with the simulation results the prototype was mounted on a test bench equipped with a cross table, a load cell, a torque sensor and a load drive. This assembly allows the measurement of forces in all three directions together with the load torque acting on the rotor.

Load capacity

First of all one coil was energized constantly at rated current. The resulting force acting on the rotor is visible in Figure 8 for certain rotation angles. The elliptical shape was expected from the finite element simulations. The difference between the 2D simulation and the measurement is about 15% originated in the axial leakage flux. It is also noteworthy that the curve is decentred. This is a result of the quadratic force component, which is negligible for the tangential component F_t but noticeable (around 5N) in radial direction (F_r) at rated current.

Motor

Additionally the driving part of the bearingless motor was tested. For this reason the motor was mechanically supported. The coils were energized by the use of vector

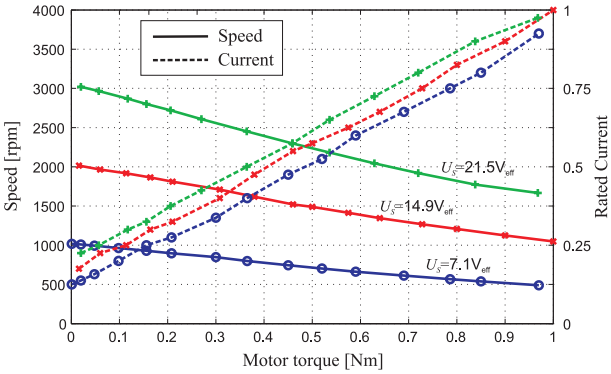

FIGURE 9 Speed-torque-characteristic of the motor

control with constant voltage. The load was increased steadily, resulting in a nearly linear decrease of the motor speed. On the other hand it is obvious that the current consumption of the motor increases. Taking a look at Figure 9, it becomes clear that the characteristic curves are similar to that of (brushless) permanent magnet excited DC machines.

Orbit

This measurement was done while the bearingless segment motor performed bearing forces and motor torque. As a matter of fact the radial deflection at certain speeds was measured and is displayed in Figure 10. The orbit is caused by unbalance. The amplitude of the orbit increases until the resonance frequency ω_3 is reached. After crossing the resonance the orbit decreases again.

Sensor Signals

Five Hall sensors were positioned in-between the stator segments to obtain the rotor angle. Figure 11 shows the signal detected by one Hall sensor. There is a

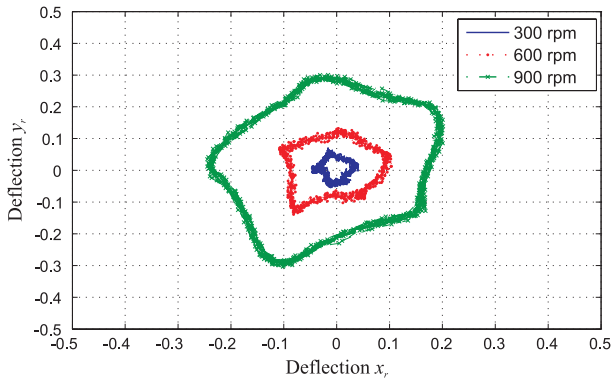

FIGURE 10 Bearingless motor in action - orbit

considerable third harmonic in this signal. So the announced transformation (16) with k=1 was used in the sensor electronics, to suppress this harmonic. In this case (m=5, p_z=6) only harmonics of the order

$$i = 5n \pm 1 \qquad n \in \mathbb{N} \tag{20}$$

remain in the signal after transformation. Figure 11 shows that the third harmonic was effectively erased.

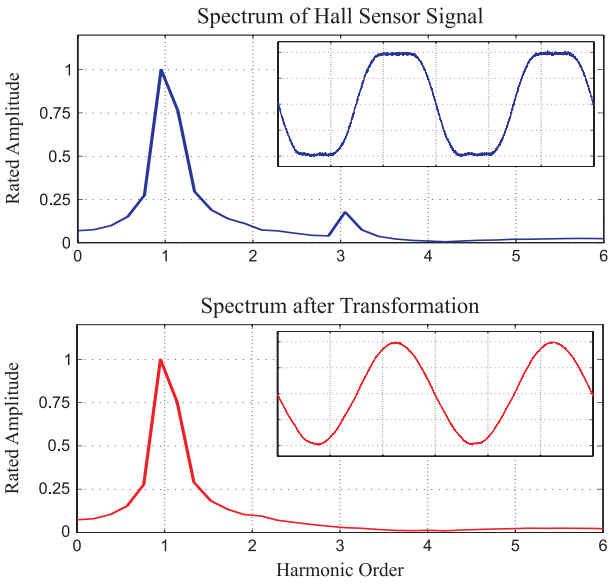

FIGURE 11 Measured and transformed Hall signal and its harmonics

SUMMARY

The design process of a bearingless segment motor with buried permanent magnets was outlined. Some motor specific details concerning the sensors and the rotor dynamics were considered. The finite element optimization was discussed and data concerning the prototype motor was given. Some of the measurements that were made with the prototype were presented in this paper. They proof the practical functionality of the theoretical considerations.

Further work that might offer interesting results could be tests concerning the field weakening capability of this motor. Moreover a new control scheme that uses the quadratic term for F_r (and not just compensates it) might be investigated. This could result in a faster response of the closed loop position controller.

ACKNOWLEDGEMENT

This research project was funded by the Austrian Science Fund (FWF) under contract P17523-N07. The authors thank the Austrian Government for the support. Scientific advisory support and parts of the control algorithms were kindly given by the Austrian Center of Competence in Mechatronics (ACCM), a K2 Centre of the COMET program of the Austrian Government.

References

1. Schöb, R. and Barletta, N., Principle and application of a bearingless slice motor, Proc. of the 5th Int. Symp. on Magnetic Bearings (ISMB5), Kanazawa, Japan, 1996
2. Gruber, W. and Amrhein, W., Design of a Bearingless Segment Motor, Proc. of the 10th Int. Symp. on Magnetic Bearings (ISMB10), Martigny, Switzerland, 2006.
3. Silber, S., Amrhein, W., Boesch, P., Schoeb, R. and Barletta, N., Design aspects of bearingless slice motors, IEEE/ASME Trans. on Mechatronics, Vol. 10 No. 6, 2005.
4. Neff M., Bearingless centrifugal pump for highly pure chemicals, Proc. of the 8th Int. Symp. on Magnetic Bearings (ISMB8), Mito, Japan, 2002.
5. Takemoto, M.; Uyama, M.; Chiba, A.; Akagi, H. and Fukao, T., A deeply-buried permanent magnet bearingless motor with 2-pole motor windings and 4-pole suspension windings, Proc. of the IEEE Ind. Applic. Conf. IAS, Vol. 2, Salt Lake City, USA, 2003.
6. Schneeberger, T. and Kolar, J. W., Novel Integrated Bearingless Hollow-Shaft Drive, Proc. of the IEEE Ind. Applic. Conf. IAS, Vol. 1, Tampa, USA, 2006.
7. Karutz, P., Nussbaumer T., Gruber W. and Kolar, J. W., The Bearingless 2-Level Motor, Proc. of the 7th Int. Conf. on Power Electronics and Drive Systems (PEDS), Bangkok, Thailand, 2007.
8. Clarke, E., Circuit Analysis of A-C Power Systems, John Wiley & Sons, Vol. 2, 1950.
9. Grabner, H., Dynamik und Ansteuerkonzepte lagerloser Drehfeld-Scheibenläufermotoren in radialer Bau-

form, Ph. D. dissertation, Johannes Kepler University Linz, Trauner Verlag, 2007.
10. Amrhein, W., Silber, S. and Nenninger, K., Levitation forces in bearingless permanent magnet rotors, IEEE Trans. on Magnetics, Vol. 35, No. 5, 1996.
11. Krämer, E., Dynamics of Rotors and Foundations, Springer-Verlag, 1993.
12. Nenninger, K., Untersuchungen zum lagerlosen Einphasen-Scheibenläufermotor, Ph. D. dissertation, Johannes Kepler University Linz, 2004.